

Magnetic-field-induced propulsion of jellyfish-inspired soft robotic swimmersR. Pramanik ^{1,2}, R. W. C. P. Verstappen,¹ and P. R. Onck ^{2,*}¹*Computational and Numerical Mathematics Group, Bernoulli Institute for Mathematics, Computer Science and Artificial Intelligence, University of Groningen, Netherlands*²*Micromechanics Group, Zernike Institute for Advanced Materials, University of Groningen, Netherlands*

(Received 28 March 2022; revised 10 November 2022; accepted 19 December 2022; published 18 January 2023)

The multifaceted appearance of soft robots in the form of swimmers, catheters, surgical devices, and drug-carrier vehicles in biomedical and microfluidic applications is ubiquitous today. Jellyfish-inspired soft robotic swimmers (jellyfishbots) have been fabricated and experimentally characterized by several researchers that reported their swimming kinematics and multimodal locomotion. However, the underlying physical mechanisms that govern magnetic-field-induced propulsion are not yet fully understood. Here, we use a robust and efficient computational framework to study the jellyfishbot swimming kinematics and the induced flow field dynamics through numerical simulation. We consider a two-dimensional model jellyfishbot that has flexible lappets, which are symmetric about the jellyfishbot center. These lappets exhibit flexural deformation when subjected to external magnetic fields to displace the surrounding fluid, thereby generating the thrust required for propulsion. We perform a parametric sweep to explore the jellyfishbot kinematic performance for different system parameters—structural, fluidic, and magnetic. In jellyfishbots, the soft magnetic composite elastomeric lappets exhibit temporal and spatial asymmetries when subjected to unsteady external magnetic fields. The average speed is observed to be dependent on both these asymmetries, quantified by the glide magnitude and the net area swept by the lappet tips per swimming cycle, respectively. We observe that a judicious choice of the applied magnetic field and remnant magnetization profile in the jellyfishbot lappets enhances both these asymmetries. Furthermore, the dependence of the jellyfishbot swimming speed upon the net area swept (spatial asymmetry) is twice as high as the dependence of speed on the glide ratio (temporal asymmetry). Finally, functional relationships between the swimming speed and different kinematic parameters and nondimensional numbers are developed. Our results provide guidelines for the design of improved jellyfish-inspired magnetic soft robotic swimmers.

DOI: [10.1103/PhysRevE.107.014607](https://doi.org/10.1103/PhysRevE.107.014607)**I. INTRODUCTION**

Soft robotics has been one of the most significant recent topics in the soft matter community due to the broad range of emerging applications in microfluidics and biomedical engineering [1–3]. From targeted drug delivery [4], to robotic surgery [5], to small-scale manipulation and labeling [6], small-scale flexible robotic swimmers have witnessed an increasing demand [7,8] owing to their swimming versatility, ergonomics, the possibility of miniaturization, adaptive surrounding fluidic interactions, and ability of multimodal locomotion [9,10].

Soft polymers or elastomer matrices are often embedded with multifunctional stimuli-responsive second-phase filler materials to induce cross-domain energy transduction [11], resulting in smart elastica [12]. For example, soft composites with exceptional magneto-responsive features have been developed for shape-morphing applications [13,14] and flexible multifunctional composites have been fabricated by combining shape memory polymers, electroactive polymers, pneumatic or electrical components together with soft matrices [15]. However, tethered electroactive and thermore-

sponsive soft robots are prone to local heating and low system efficiency due to additional onboard compartments and intricate wiring systems.

In contrast, magnetic actuation is a noncontact mode manipulation, which is often preferred for *in vivo* biomedical and microfluidic applications [16,17]. Untethered actuation and noninvasive remote control with high precision have paved the way for the development of magnetic soft robotic swimmers [18,19] for use in drug delivery, catheterization, endoscopy, and laparoscopic surgery [20,21]. These miniature soft robots have been shown to exhibit adaptive and multimodal locomotion under external magnetic fields [22].

For instance, terrestrial locomotion has been demonstrated for bioinspired soft magnetic millirobots [23]. Magnetic soft robots have been successfully employed as efficient aquatic carrier vehicles to exhibit versatile locomotion and adaptive swimming dynamics [24,25]. In most cases, these flexible robots are inspired by nature [26], ranging from miniature microtubule-based structures such as cilia [27] and flagella [28], to spermatozoa [29] and jellyfish [30]. In general, soft robotic swimmers have a strong biological inspiration from fish [31,32], squids [33], turtles [34], and jellyfish [35,36].

In a marine environment, jellyfish are arguably the most efficient aquatic swimmers [37], because they require the lowest

*Corresponding author: p.r.onck@rug.nl

cost of transport and energy expenditure (per unit mass) during their locomotion [38]. This has been a strong motivation for the recent development of jellyfishbots [9,39,40]. For instance, a soft jellyfishbot was fabricated using hard magnetic neodymium-iron-boron (NdFeB) microparticles embedded within a soft silicone elastomer [9]. Its ability to shape morph under external magnetic actuation and its swimming kinematics have been recently reported [40]. Similarly, a biomimetic jellyfish-inspired robot has been fabricated using shape memory alloy [41] and soft pneumatic composites [42].

However, these studies have primarily focused on fabrication techniques or experimental characterization to estimate swimming performance. Clearly, there is a need for a fundamental understanding and numerical modeling of their magnetic-field-induced propulsion. Studies have been performed using computational fluid dynamics-based optimization and control to estimate the swimming kinematics of flexible robotic fish [7] and soft robotic sperm [43]. The nonlinear coupled interactions between inertia, viscosity, and elasticity have been studied for highly deformable robotic actuators within a fluidic network [44,45].

In other studies, the discrete elastic rod method was used to predict the structural kinematics of soft robotic swimmers [46], the propulsion of compliant magnetic nanowires has been analyzed using a bead-spring model to incorporate both the large deformation geometric nonlinearity and the associated hydrodynamic interactions [47], and the multiphysics coupling behavior of a magnetically propelled fish-inspired robotic swimmer has been studied using COMSOL [48]. In addition, several efficient numerical techniques have been used, such as the finite element method [49], boundary element method [27], and lattice Boltzmann method [50] (to name a few), for predicting the overall system dynamics and spatiotemporal evolution of the state variables.

Although several modeling approaches have been undertaken, a robust computational model involving multiphysics of large-deformation two-way fluid-solid coupling with a complete Navier-Stokes implementation, while simultaneously solving for the magnetodynamics, has never been used to study the swimming kinematics of robotic swimmers. This is the aim of the present paper and the objectives are to (a) understand the swimming kinematics and magnetic-field-induced locomotion of an experimental system of a soft smart jellyfishbot reported in a recent study [40]; (b) perform a rigorous computational design through numerical simulation using a coupled computational multiphysics model involving the magnetics, solid mechanics, fluid dynamics, and large deformation fluid structure interaction (FSI) [51]; (c) develop functional relationships between different kinematic variables and nondimensional numbers; and (d) explain the jellyfishbot locomotion based on the spatial and temporal breaking of symmetry.

We discuss the underlying physical mechanisms that govern the magnetically actuated jellyfishbot through the use of a robust fluid-structure interaction magnetodynamics model that allows the jellyfishbot to be able to handle large Reynolds number flows incorporating solid and fluid inertial effects [52]. We explain the relative contribution of inertial, magnetic, viscous, and elastic forces in determining the jellyfishbot swimming kinematics.

The present paper is organized as follows: the computational framework for the coupled multiphysics problem is presented in Sec. II. The magnetodynamics large-deformation FSI model, along with appropriate boundary conditions and solution techniques, is discussed. The results of numerical simulations are reported in Sec. III. The jellyfishbot lappet material properties and swimming kinematics are discussed. Section IV addresses the influence of the structural, fluidic, and magnetic properties on the kinematic performance. Section V presents the nondimensional numbers and their correlation with jellyfishbot kinematic parameters. Here, the functional relationships between the different kinematic parameters are reported as well. Finally, Sec. VI concludes the paper.

II. COMPUTATIONAL FRAMEWORK

The jellyfishbot lappets are considered to be composed of silicone elastomer impregnated with hard magnetic NdFeB microparticles in equal mass ratios of 1:1 (please refer to [9] for details). During fabrication, strong external magnetic fields are exerted to generate a remnant magnetization profile M_r along the lappet length s . Magnetic body torques are generated due to remnant magnetization in the flexible lappets. The uniform magnetic field acts directly upon the jellyfishbot in an untethered and remote manner. This allows them to deform and displace the surrounding fluid and exhibit net propulsion (see Fig. 1).

The jellyfishbot lappets are intended to deform in a flexural manner when subjected to uniform external magnetic fields; there are no spatial gradients for this field. In addition (for the sake of simplicity), we assume that the jellyfishbot soft robotic swimmer is essentially composed of only the two symmetric lappets—where one end of each lappet is free, while the other ends are connected to each other at the jellyfishbot center, which ideally constitutes the jellyfishbot body (here, a point in space). And then, these lappets could be visualized as highly flexible cantilever beams that can vertically translate [9,40]. Furthermore, both the lappets are (permanently) magnetized throughout their entire length using sinusoidal profiles of the remnant magnetization [see Fig. 2(a)]. Subject to external magnetic actuation, the generated body torques (equivalent to the local magnetic moments) act upon the lappets.

However, the field does not move with the jellyfishbot. Rather, it is uniform and has the same strength everywhere throughout the computational domain of interest. The jellyfishbot is maneuvered through a viscous fluid and spatiotemporally controlled by an external time-varying (unsteady, but uniform) oscillating magnetic field along the y axis (Fig. 1), during which the lappets undergo flexural deformation to displace the surrounding fluid and generate thrust required for locomotion.

When the system of interest involves multiple physical domains such as magnetics, fluid dynamics, and solid mechanics along with large deformation FSI, closed-form analytical solutions are not obtainable. One has to resort to numerical techniques and computational models in order to obtain numerical solutions of the coupled sets of nonlinear partial differential equations. In the present paper, magnetics, fluid mechanics, and solid dynamics are strongly coupled and act

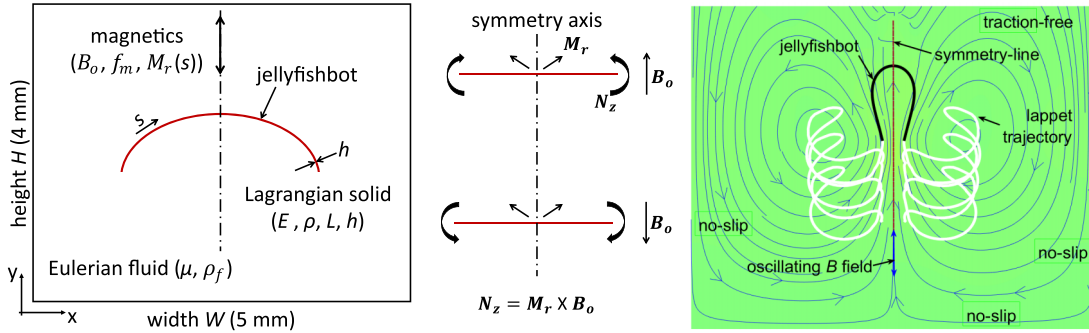


FIG. 1. Left: Solid and fluid domains, jellyfishbot—magnetic, solid, and fluid properties. Center: Note that the initial, undeformed configuration (without the magnetic field) is a flat plate. Right: Schematic representation of the jellyfishbot trajectory, boundary conditions, and the streamlines in the fluid. The external oscillating magnetic field is a uniform unsteady field in the y direction with no spatial gradient, shown by the two-sided blue arrow.

coherently to influence the evolution of structural kinematics and flow dynamics. To address this complexity, we use a robust two-dimensional computational model [52] using a fixed-grid fictitious domain method to account for the multiphysics involved in these magnetically actuated jellyfishbots.

We aim to understand the relative importance of the individual system parameters on jellyfishbot swimming speed, and also study the interplay of inertia, viscous, magnetic, and elastic forces that dictate the jellyfishbot swimming kinematics. Appropriate boundary conditions in the form of no-slip, no-penetration, and traction continuity are enforced using Lagrange multipliers at the fluid-solid interface. The velocity of the fluid is equated to that of the solid at the interface using a point-collocation technique [53].

A. Solid dynamics

The jellyfishbot consists of two equal-sized lappets that are modeled as a discrete assemblage of two-dimensional homogeneous, isotropic, linearly elastic Euler-Bernoulli beams. The lappets are slender with a very high slenderness ratio; specifically, $L/h = 1000$, where L and h represent the lappet length and thickness, respectively. Since the jellyfishbot lappets undergo large deformation, the strain is geometrically nonlinear and the beam curvature is high. These factors coherently lead us to choose a nonlinear form for the axial strain [see Eq. (2)], which is a standard formulation often

used in nonlinear finite element analysis for nonlinear strain terms [54].

Geometric nonlinearity is taken into account using an updated Lagrangian formulation. The principle of virtual work is used as the starting point for the finite element formulation [55]. The virtual work of the external forces at time $t + \Delta t$ ($\delta W_{\text{ext}}^{t+\Delta t}$) is equated to the virtual work of the internal forces ($\delta W_{\text{int}}^{t+\Delta t}$). The internal virtual work is written as [49]

$$\delta W_{\text{int}}^{t+\Delta t} = \int_V (\sigma \delta \epsilon + \rho (\ddot{u} \delta u + \ddot{v} \delta v)) dV. \quad (1)$$

Here, ρ represents the beam density, σ and $\delta \epsilon$ represent the axial stress and virtual strain in the beam element, and dV represents the elemental volume. The Lagrangian displacement components for the beam elements along the horizontal and vertical directions are denoted by u and v , respectively. The first component at the right-hand side in Eq. (1) represents the potential energy in the beam element due to the mechanical deformation that the jellyfishbot lappets undergo. The second term (which is a product of the beam density, acceleration, and elemental volume) accounts for the kinetic energy of the beam element. Correspondingly, the nonlinear axial strain ϵ in the beam is given by

$$\epsilon = \frac{\partial u}{\partial x} + \frac{1}{2} \left(\frac{\partial v}{\partial x} \right)^2 - y \frac{\partial^2 v}{\partial x^2}. \quad (2)$$

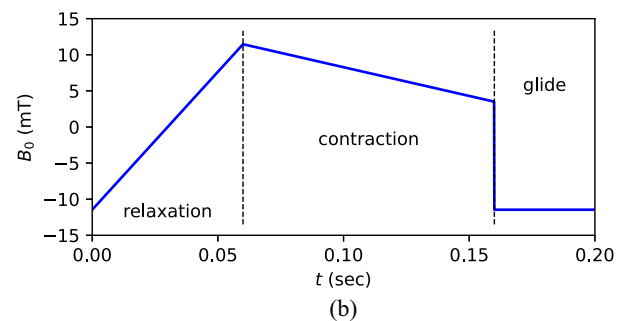
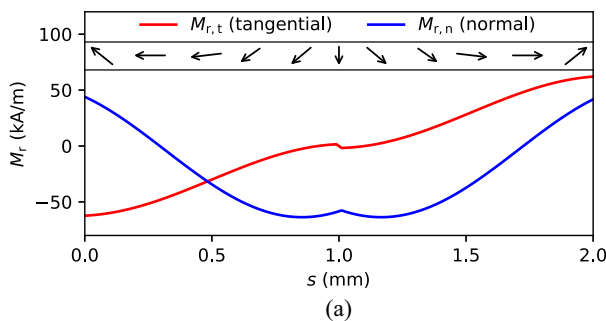


FIG. 2. (a) Variation of jellyfishbot remnant magnetization M_r with respect to the curvilinear axis s ; the black arrows indicate the direction of M_r at specific segments along the jellyfishbot length. (b) Variation of B_0 with time t indicating different phases of jellyfishbot swimming kinematics.

The external virtual work is represented as

$$\delta W_{\text{ext}}^{t+\Delta t} = \int \left(f_x \delta u + f_y \delta v + N_z \frac{\partial \delta u}{\partial x} \right) A dx + \int (t_x \delta u + t_y \delta v) b dx. \quad (3)$$

Here, f_x and f_y are the magnetic body forces in the axial and transverse directions, respectively, A represents the cross-sectional area of the beam element, N_z denotes the magnetic body couple in the out-of-plane direction, t_x and t_y represent the surface tractions, and b is the out-of-plane thickness. The principle of virtual work is linearized [56] and discretized to obtain

$$\delta \mathbf{p}^T (\mathbf{K} \Delta \mathbf{p} + \mathbf{M} \ddot{\mathbf{p}}^{t+\Delta t} - \mathbf{F}_{\text{ext}}^{t+\Delta t} + \mathbf{F}_{\text{int}}^{t+\Delta t}) = 0. \quad (4)$$

Here, the \mathbf{K} matrix combines both the material and geometric stiffness, \mathbf{M} denotes the mass matrix, $\mathbf{F}_{\text{ext}}^{t+\Delta t}$ and $\mathbf{F}_{\text{int}}^{t+\Delta t}$ represent the external and internal force vectors, respectively, $\Delta \mathbf{p}$ is the nodal displacement increment vector, and $\ddot{\mathbf{p}}$ denotes the nodal acceleration vector.

Temporal discretization of the nodal acceleration vector is performed using Newmark's algorithm [57] such that Eq. (4) can be written in terms of the beam velocity. Newmark's integration scheme has often been used in finite element analysis to model dynamical systems [58]. Here we use it to integrate Eq. (4). It is an explicit method that guarantees unconditional stability and second-order accuracy for nonlinear systems [59]. This allows us to use a larger time step.

For Newmark's integration scheme, the range of these parameters is as follows: $0 \leq \gamma \leq 1$ and $0 \leq \beta \leq 0.5$. We consider Newmark's integration parameters $\gamma = 1.0$ and $\beta = 0.5$ for our present paper, which is a standard and optimized choice made by several researchers to achieve numerical stability and convergence [60–62]. For more details on the discretized equations of motion for the solid mechanics model, see [62].

B. Magnetostatics

In our paper, the jellyfishbot multifunctional composite is considered to be a permanently magnetic material. The (remnant) magnetization \mathbf{M} of the jellyfishbot lappets is known *a priori* in every beam element, and this value is a constant. A change in the external magnetic field has no influence on its magnitude. Furthermore, the constitutive relation considered here is $\mathbf{B}_o = \mu_o (\mathbf{M} + \mathbf{H}_o)$, where \mathbf{B}_o is the magnetic flux density, \mathbf{H}_o is the applied (prescribed) magnetic field, and μ_o is the permeability of vacuum (with a constant value of $12.57 \times 10^{-7} \text{ N/A}^2$). Next, we evaluate N , the magnetic couple per unit volume, using the relation $N = \mathbf{M} \times \mathbf{B}_o$.

The numerical simulations and computational analyses are two dimensional. The only nonzero component of the magnetic body couple is the out-of-plane component N_z , which is the source for the external virtual work in Eq. (3). Since the applied magnetic field is uniform throughout the entire computational domain, the magnetic body forces due to the field gradients are zero.

C. Fluid mechanics

The flow field surrounding the swimming jellyfishbot is unsteady and nonuniform. Therefore, we solve for the complete Navier-Stokes equation involving the inertial, convection, pressure, and diffusion terms. The fluid is assumed to be Newtonian and incompressible. Considering the mass and linear momentum balance, the physical behavior of the fluid is captured through the following equations:

$$\nabla \cdot \mathbf{u} = 0, \quad (5)$$

$$\rho_f [\dot{\mathbf{u}} + (\mathbf{u} \cdot \nabla) \mathbf{u}] = -\nabla p + 2\mu \nabla \cdot \mathbf{D}. \quad (6)$$

Here, p represents the scalar pressure field, \mathbf{D} denotes the rate of deformation tensor, and \mathbf{u} is the velocity field. μ and ρ_f represent the fluid viscosity and density, respectively.

Equations (5) and (6) are solved using Eulerian finite elements by a Galerkin method. The fluid domain is discretized into quadrilaterals; in this paper, we use the Taylor-Hood Q_2Q_1 elements, in which the velocity and pressure of the fluid are interpolated quadratically and linearly, respectively [63]. The velocity is calculated at the vertices, midsides, and midpoint of the quadrilateral, while the pressure is calculated at the vertices.

D. Fluid-solid coupling

The solid and fluid domains are coupled by imposing the constraint that the velocity at the nodes of the solid beam is equal to the velocity of the surrounding fluid:

$$\mathbf{u} = \dot{\mathbf{p}}. \quad (7)$$

This coupling [Eq. (7)] is established with the help of Lagrange multipliers' mortar elements using the fictitious domain method. For further details on the Eulerian finite element model and the coupling procedure, see [52,64].

E. Boundary conditions

The computational domain is two dimensional and has a dimension of 5 mm (width) by 4 mm (height). The flow fields and structural dynamics are symmetrical about the jellyfishbot central (longitudinal) axis, which is also the axis of symmetry for the problem definition. The jellyfishbot initial velocity is assumed to be zero. It has an undeformed initial configuration, in which the jellyfishbot is fully straight (like a flat plate) and oriented horizontally.

The flow field is symmetric about the jellyfishbot center due to both the structural and kinematic symmetries of the jellyfishbot (see Fig. 1). Thus, symmetric boundary conditions are imposed at the center line. The top end of the computational domain is traction free, and the bottom, left, and right ends of the computational domain are considered no-slip no-penetration boundaries. Although the magnetic field does not vary in space, it still has a temporal variation as shown in Fig. 2(b).

F. Solution procedure

The external magnetic actuation and, consequently, the jellyfishbot propulsion are along the y axis (see Fig. 1). The

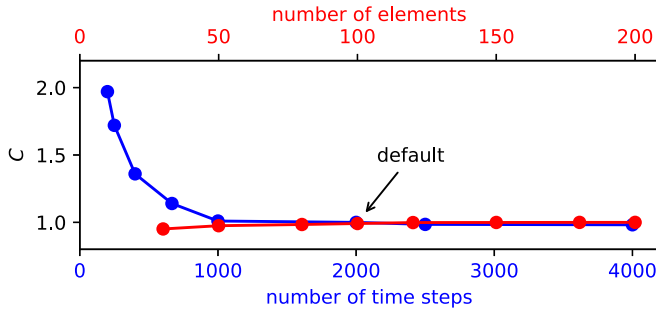


FIG. 3. Convergence study on the reference case shown in Figs. 1, 2, 4, and 5 to ensure the numerical framework is stable: the system variable of interest (here, the normalized jellyfishbot swimming speed C) asymptotically attains a constant value with an increase in the number of beam elements (i.e., decreasing mesh size), and increase in the number of time steps (i.e., decreasing time step).

magnetic body couple acting on the jellyfishbot is calculated from the magnetic field. The magnetic body couple is fed as an external load to the coupled solid-fluid model. This simultaneously solves for the jellyfishbot velocity, as well as the velocity and pressure fields of the surrounding fluid. Next, the jellyfishbot velocity is integrated using Newmark’s algorithm to obtain its new position, and this procedure is repeated.

G. Implementation

The present paper was implemented using an in-house FORTRAN code based on a finite element numerical framework [27]. All the numerical simulations reported henceforth were run on a high-performance computing cluster. To begin with, we perform a numerical convergence study to ensure the model stability (see Fig. 3).

As a starting choice, the number of beam elements considered is 100. The time step is chosen to be 0.1 ms. This combination holds true for all the cases studied henceforth. For numerical convergence, we vary the time step keeping the mesh size constant, and vice versa. From Fig. 3, we observe that with increasing the number of elements (decreasing the mesh size) or decreasing the time step, the value of C asymptotically attains a constant value.

III. RESULTS AND DISCUSSION

A. System parameters

The geometric variables are the jellyfishbot lappet length (L) and thickness (h); the material properties are Young’s modulus (E) and density (ρ); then, there is fluid viscosity (μ) and its density (ρ_f). We also have the external magnetic field (\mathbf{B}_0), remnant magnetization (\mathbf{M}_r) with its tangential ($M_{r,t}$) and normal ($M_{r,n}$) components, and the actuation frequency (f_m). The cycle time period (t_{ref}) is the inverse of f_m .

B. Kinematics

We perform two-dimensional simulations to study the jellyfishbot kinematics, with the aim to provide a qualitative comparison with real-life jellyfish and their experimental counterpart. Their kinematic behavior, especially the bending

motion of the lappets and their asymmetric strokes, are similar and we account for three distinct phases that exist during a swimming cycle: relaxation, contraction, and glide. The inertial effects give rise to the glide phase, which is prominently present in both the experimental systems and the numerical simulation results.

The lappet deformation behavior, consisting of the combined spatial and temporal asymmetries, results in net propulsion. In addition, the magnetic field used in the model [see Fig. 2(b)] is similar to that used in experimental studies [9,40]: it is assumed to be uniform throughout space (with no spatial gradient) but varies with respect to time. Also, the vortex fields generated (see Fig. 4) due to the jellyfishbot lappet deformation have a strong qualitative agreement with the experimental studies (see, e.g., [9,40]).

We study the strongly coupled FSI arising due to large lappet displacement, jellyfishbot swimming, and propulsion through the viscous fluid. The jellyfishbot swimming kinematics and the lappet trajectory for one complete swimming cycle (for the reference case) are shown in Fig. 5. Here, the values for the system parameters are $E = 0.1845$ MPa, $L = 2.0$ mm, $\rho = 1.7 \times 10^5$ kg/m³, $h = 0.065$ mm, $\mu = 0.1$ Pa s, $\rho_f = 1500$ kg/m³, and $f_m = 5.0$ Hz. Furthermore, the Reynolds number for the reference problem is 0.3. The variation of \mathbf{M}_r with respect to length and the variation of the external, untethered, unsteady, uniform, oscillating magnetic field \mathbf{B}_0 with time are shown in Figs. 2(a) and 2(b), respectively.

Jellyfish propulsion comprises three lappet motions (also called strokes or phases), and these are characterized by the up-and-down flexural beating of their elastomeric lappets. From another viewpoint, these are also the recovery (upward relaxation) and the effective (downward contraction) strokes, respectively. In addition to this, there is the glide phase after the completion of the recovery and effective phases, during which the jellyfishbot propels forward without any noticeable structural (lappet) deformation. The net displacement per cycle is a sum of the contributions from the distances traversed by the jellyfishbot during these three individual phases.

For the reference case, the displacement is shown for ten cycles in Fig. 6(a) with $t_{\text{ref}} = 0.2$ s for one swimming cycle in Fig. 6(b). Clearly, a steady state is observed with a constant value of $c = 2.07$ mm/s. In this paper, we exclusively report the steady-state velocities unless mentioned otherwise.

C. Symmetry-breaking mechanisms

For real-life aquatic jellyfish as well as jellyfishbots, the spatial and/or temporal symmetry breaking of their flexible lappets is essential for thrust generation and propulsion [66]. When the fluid displaced due to flexural deformation of the lappets during the contraction (effective) stroke is higher than that during the relaxation (recovery) stroke, it results in a higher swept area during the former as compared to the latter. This difference in the areas swept during these phases gives rise to the “spatial asymmetry” and a net forward jellyfishbot displacement. In other words, it is also the breaking of spatial symmetry during which the flexible lappets have a nonreciprocal motion for the contraction and relaxation strokes.

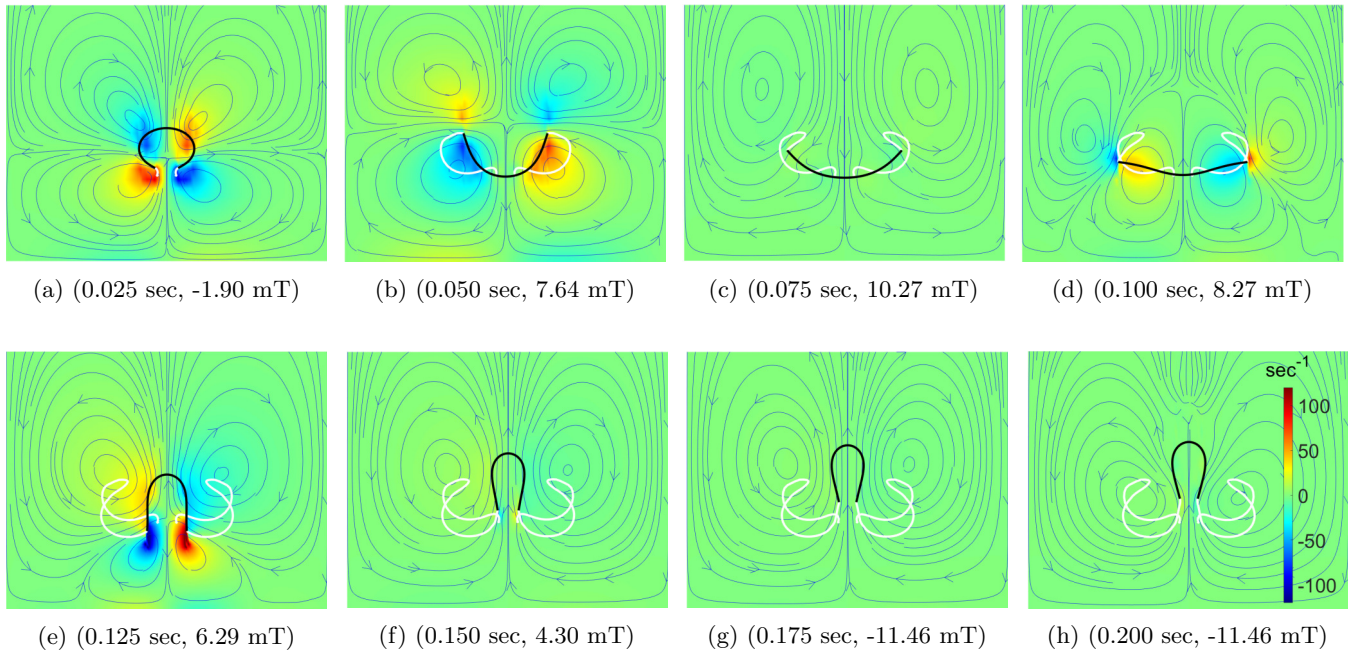


FIG. 4. Chronological sequence of jellyfishbot configurations and surrounding vortex field through the streamlines and magnitude of the vortex field; (\cdot, \cdot) represents the applied magnetic field and the corresponding cycle time, respectively (t, \mathbf{B}_0) . For an animation of the swimmer, see movie S1 in the Supplemental Material [65].

The glide phase thereafter adds on to the jellyfishbot kinematics using inertial effects. When the time required for the effective stroke is lower than compared to the recovery stroke, a net forward jellyfishbot displacement is observed. This is attributed to the breaking of the temporal symmetry, and is referred to as “temporal asymmetry.” This occurs when there is a predominant existence of the glide phase. Furthermore,

(higher) inertial effects contribute to an increased temporal asymmetry [67]. Both these asymmetries are utilized by the jellyfishbots for efficient and versatile locomotion and enhanced swimming performance.

The fluid dynamics also influence the asymmetries, and they can potentially have an important contribution to efficient jellyfishbot propulsion. By taking a close look at Fig. 4, we

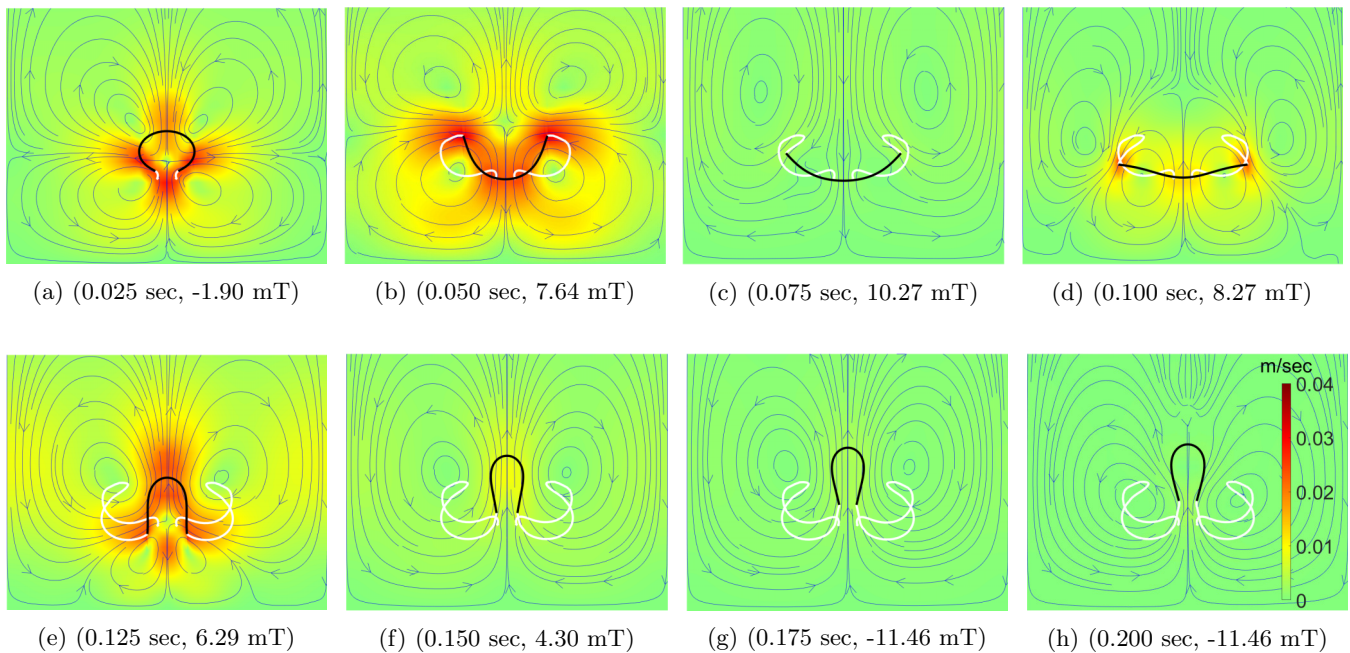


FIG. 5. Chronological sequence of jellyfishbot configurations and surrounding velocity field through the streamlines and magnitude of the velocity field; (\cdot, \cdot) represents the applied magnetic field and the corresponding cycle time, respectively (t, \mathbf{B}_0) . For an animation of the swimmer, see movie S2 in the Supplemental Material [65].

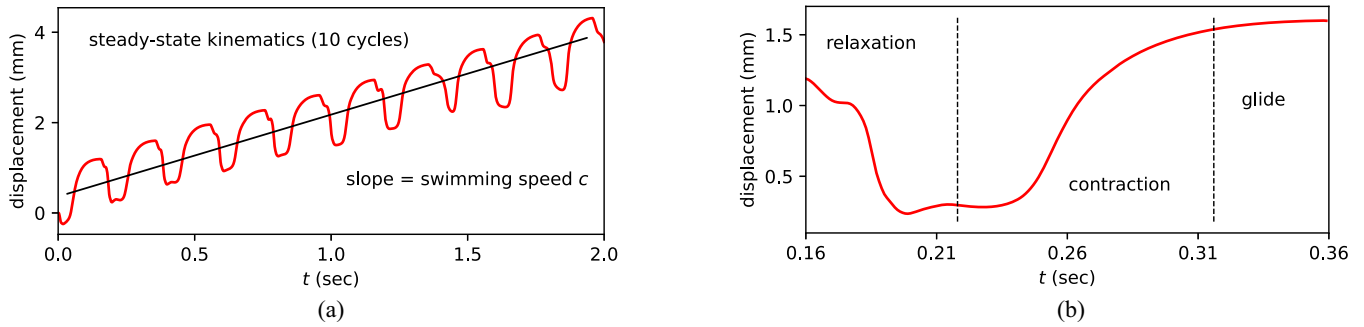


FIG. 6. (a) Steady-state kinematics of the reference jellyfishbot swimmer of length $L = 2.0$ mm for ten cycles. (b) Jellyfishbot displacement showing the three individual phases for one cycle (time period is 0.2 s).

observe a vortex ring generated during the contraction stroke, which propagates down the lappets. As soon as the next cycle starts, there is a generation of small vortices during the recovery stroke. However, the Reynolds number here is relatively small (from 0.1 until 0.7) and thus the inertial effects are negligible. As a result, the vortices do not interact with one another, and their influence upon the jellyfishbot swimming kinematics is minimal.

D. Wall proximity

Another aspect that plays a significant role during jellyfishbot locomotion is the wall proximity. The jellyfishbot is primarily intended to locomote through confined regions to mimic the real-life situation of a soft robot swimming through blood vessels or narrow vascular channels [10]. In such cases, the assumption of no-slip no-penetration proximal boundaries holds true, and the effect of wall proximity is important.

To investigate this, we perform numerical simulations for a jellyfishbot of length $L = 2.0$ mm for different dimensions of the computational domain, so that the horizontal proximity of the left and right boundaries, and the vertical proximity of the bottom boundary, are varied in the undeformed configuration to understand the horizontal and vertical wall effects, respectively. Our findings are plotted in Fig. 7.

We observe that the wall proximity has an important effect on the swimming speed at small proximities (see Fig. 7). We note that the jellyfishbot average speed asymptotically converges upon increasing the vertical and lateral proximities,

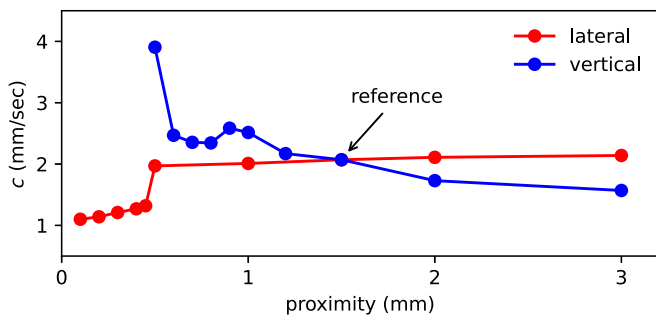


FIG. 7. Variation of jellyfishbot average speed c with respect to lateral and vertical proximity using a vertical proximity of 0.5 mm for the lateral variation, and a lateral proximity of 1.5 mm for the vertical variation.

beyond a value of approximately 1.5 mm. We use this value of wall proximity for all the cases we study henceforth to eliminate wall effects for the swimmer with $L = 2.0$ mm. It is interesting to note that decreasing the lateral proximity reduces the jellyfishbot speed, while the effect is the opposite in the case of the vertical proximity.

The results show that, when a robotic swimmer is intended to traverse through very narrow tubular channels whose dimensions are comparable to that of the swimmer dimensions, the wall proximity and the wall’s cross-sectional morphology have a very important role to play and, therefore, the boundary effects should not be ignored. Although we do not discuss the interface effects or locomotion near fluid surfaces in the present paper, it would nonetheless be important to understand its influence on the jellyfishbot swimming kinematics. However, we leave this to future work.

E. Swept area and glide

The area swept due to lappet deformation during individual phases in a swimming cycle is directly proportional to the net fluid area propelled (refer to [62] for details). We characterize the shape and size of the swept areas using the normalized area swept (NAS), defined as the ratio of the area swept by the tip of the jellyfishbot (see Fig. 8) to the area of the circle with diameter $L/2$. The swept area is computed using MATLAB by evaluating the difference between the area under the curves for the effective and the recovery strokes. Breaking of trajectory symmetry gives rise to a nonzero value of net area swept per swimming cycle. The area enclosed within the trajectory of

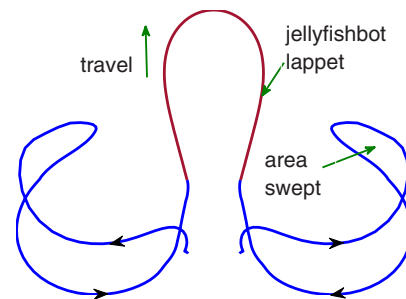


FIG. 8. Schematic representation of the area swept by the jellyfishbot lappets per swimming cycle: blue lines show the lappet trajectory.

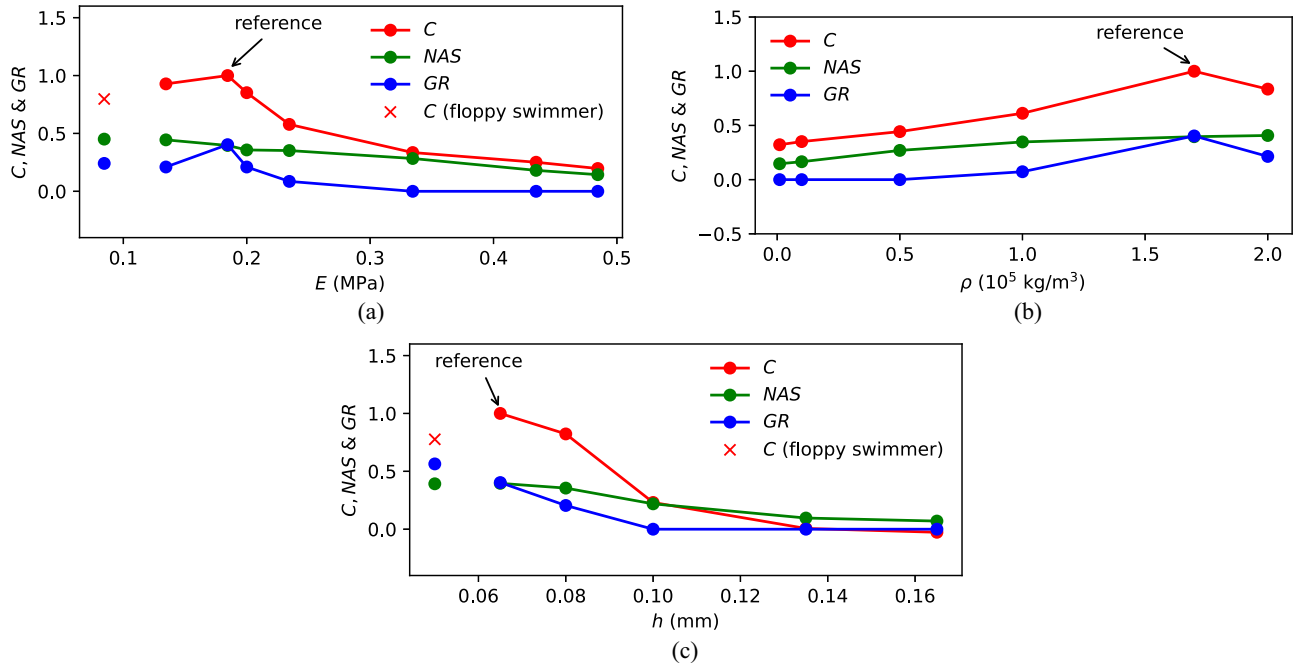


FIG. 9. Variation of C , NAS , and GR with respect to (a) E , (b) ρ , and (c) h .

the lappet tips is the net swept area. The other important parameter is the displacement that the jellyfishbot spends in the glide phase (g). This is characterized by the glide ratio (GR), defined as the ratio of g to d , where d is the jellyfishbot net steady-state displacement per swimming cycle. We also introduce a nondimensional parameter C to represent the ratio of the jellyfishbot average speed in a swimming cycle to the value of c obtained for the steady-state swimming speed in the reference case.

IV. PARAMETRIC STUDY

We perform a parameter sweep for all the system parameters and analyze how the jellyfishbot kinematics in terms of C , NAS , and GR change accordingly, and in doing so, we aim to strike the optimum kinematic performance for each individual parameter. For all the cases studied, the reference swimmer is used as a basis, and we vary one parameter at a time.

First, the structural properties are discussed, wherein the effects of jellyfishbot lappet compliance, density, and thickness are elaborated. Then, the influence of viscosity and density of the surrounding fluid is studied. Finally, the dependence of the jellyfishbot kinematics upon the external magnetic field and remnant magnetization is explained.

A. Structural properties

Young’s modulus of the jellyfishbot lappet is varied to understand its influence upon the swimming kinematics [see Fig. 9(a)]. High lappet compliance results in large deformation subject to the same magnetic actuation. Not only does this generate larger swept areas in each cycle, but it also generates a higher thrust. Consequently, this leads to an increased kinematic contribution during the glide phase. High stiffness corresponds to higher flexural rigidity, which hinders large

lappet deformation to displace the surrounding fluid. With increasing stiffness, the lappet deformation reduces and this decreases the net area swept. Thus, the jellyfishbot traverses a lower distance per cycle with a reduction in its swimming speed as well.

For very low values of lappet stiffness, excessive structural deformation is observed. This causes the soft robotic swimmer to self-coil. This coiled lappet morphology further results in a floppy swimmer, that is unable to reopen its lappets, or show any characteristic jellyfishbot kinematics [indicated by x in Fig. 9(a)]. Also, it does not exhibit a steady-state motion. The value of C (0.8) for the floppy swimmer is obtained in the first cycle. Hence, it is important to come up with an optimum value of the lappet Young’s modulus ($E = 0.1845 \text{ MPa}$), wherein both the glide and swept areas (and, consequently, the average speed) are maximum [see Fig. 9(a)]. Note that the normalized swimming speed C scales more strongly with the glide ratio GR than with the normalized swept area NAS .

Inertia is linearly proportional to the density, of a given system volume. Thus, density affects the distance traversed by the jellyfishbot through inertial effects. The jellyfishbot is able to swim a greater distance during the glide phase with an increase in inertia [see Fig. 9(b)]. When the density of the swimmer is of the same order as that of the surrounding fluid, inertial effects are negligible. This is when spatial asymmetry is the only driving force for forward propulsion since temporal asymmetry is insignificant. However, when the lappet density is considerably higher than that of the surrounding fluid, inertial effects become dominant, and we observe a higher average speed [see Fig. 9(b)].

With an increase in inertia, not only the net swept area increase but also the glide displacement is higher; this is attributed to inertia gained by the jellyfishbot in the contraction phase. Further, the area swept during the contraction phase

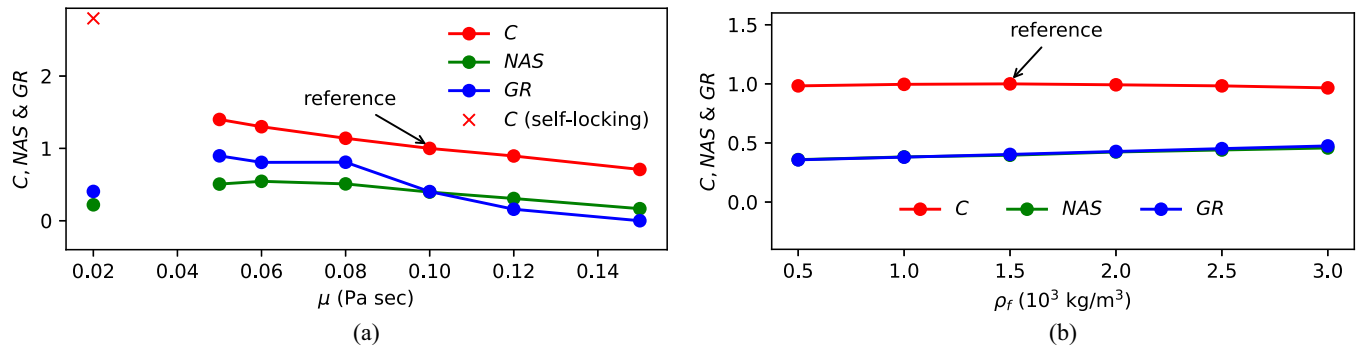


FIG. 10. Variation of C , NAS , and GR with respect to (a) μ and (b) ρ_f .

is considerably higher than that during the relaxation phase, due to inertia gained from the earlier cycles. Note that the normalized swimming speed C scales more strongly with the glide ratio GR than with the normalized swept area NAS .

An increase in lappet thickness results in an increase in flexural rigidity [see Fig. 9(c)]. The lappet deformation decreases with increased thickness due to reduced compliance. This leads to a reduction in the areas swept during the individual phases. Thus, spatial asymmetry provides the jellyfishbot with insufficient net area swept to exhibit any considerable forward propulsion. Thus, we observe a decrease in the jellyfishbot kinematic performance.

Very low values of lappet thickness mean extremely high lappet flexural compliance. This leads to an excessive and nonuniform structural deformation of the jellyfishbot. This results in a coiled jellyfishbot morphology, which is incapable of any further locomotion or swimming kinematics (a floppy swimmer, denoted by x). The value of C for the floppy swimmer (0.38) is only obtained in the first cycle; no steady-state swimming speed is reached. Consequently, an optimum lappet thickness for the best jellyfishbot kinematics could be estimated from Fig. 9(c). The effects of lappet thickness and lappet stiffness are similar because both these parameters affect the lappet flexural rigidity. The bending stiffness scales with h^3E , which ultimately determines the lappet structural deformation. Thus, Figs. 9(c) and 9(a) have a similar variation.

B. Fluid properties

Fluid viscosity strongly influences the jellyfishbot lappet deformation, since this dictates the resistance offered by the surrounding fluid during the lappet movement in the relaxation and contraction phases. During the glide phase, the jellyfishbot traverses through the fluid without any noticeable structural deformation under Stokes drag, and this is when the fluid viscosity plays a dominant role. It retards the jellyfishbot momentum and this directly reflects upon the swimming speed. With an increase in μ , the contribution from the glide phase decreases considerably, and vice versa. This is in conjunction with the observation in Fig. 10(a). Note that the normalized swimming speed C now scales more strongly with the normalized swept area NAS than with the glide ratio GR .

We observe a gradual speed reduction with an increase in viscosity because the swept areas decrease owing to less lappet deformation. The surrounding fluid resists the lappet

deformation to a higher extent. Even if the lappets move in a similar trajectory as the reference case, the resulting flow dynamics are not the same and do not influence the jellyfishbot propulsion to a major extent. Thus, the jellyfishbot kinematic performance reduces. With low values of fluid viscosity, drag and fluid resistance decrease. For a value of viscosity as low as 0.02 Pa s, lappet self-locking and vulnerability of early lappet closure become possible, further leading to an uncharacteristic jellyfishbot locomotion (denoted by x). The relatively high value of C for the floppy swimmer (2.75) is only obtained in the first cycle; no steady-state swimming speed is reached.

When the fluid viscosity is very low, the lappets deform excessively and often get locked during the contraction phase. Only when the magnetic field is reduced, the lappets can spring back. This intermediate locked structure due to the self-closure of the deformable lappets is referred to as “self-locking” [see Fig. 11(a)].

The jellyfishbot propels forward by pushing the surrounding fluid backward using its deformable lappets. The area swept by the lappets during one swimming cycle is proportional to the quantity of fluid displaced by the lappets [62]. Furthermore, the jellyfishbot swimming speed increases when the normalized area swept NAS is higher (due to spatial asymmetry, as explained earlier). The flow patterns are quite similar for all the cases analyzed. Hence, during the parametric study, we only report the value of NAS with a systematic variation in all the different system parameters.

The jellyfishbot kinematics is negligibly influenced by the density of the surrounding fluid. The effects are minimal, and we observe the variation of fluid density to affect the jellyfishbot swimming speed by less by 2% [see Fig. 10(b)].

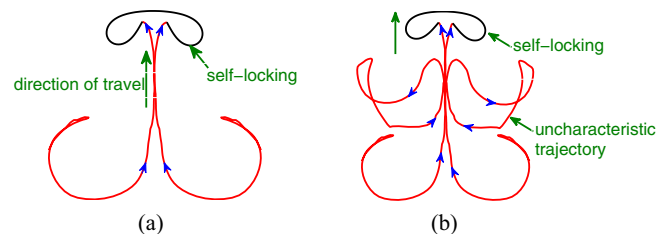


FIG. 11. Schematic representation of the jellyfishbot undergoing ephemeral closure of flexible lappets, or self-locking, when the fluid viscosity is too low (a) or the magnetic field is too high (b).

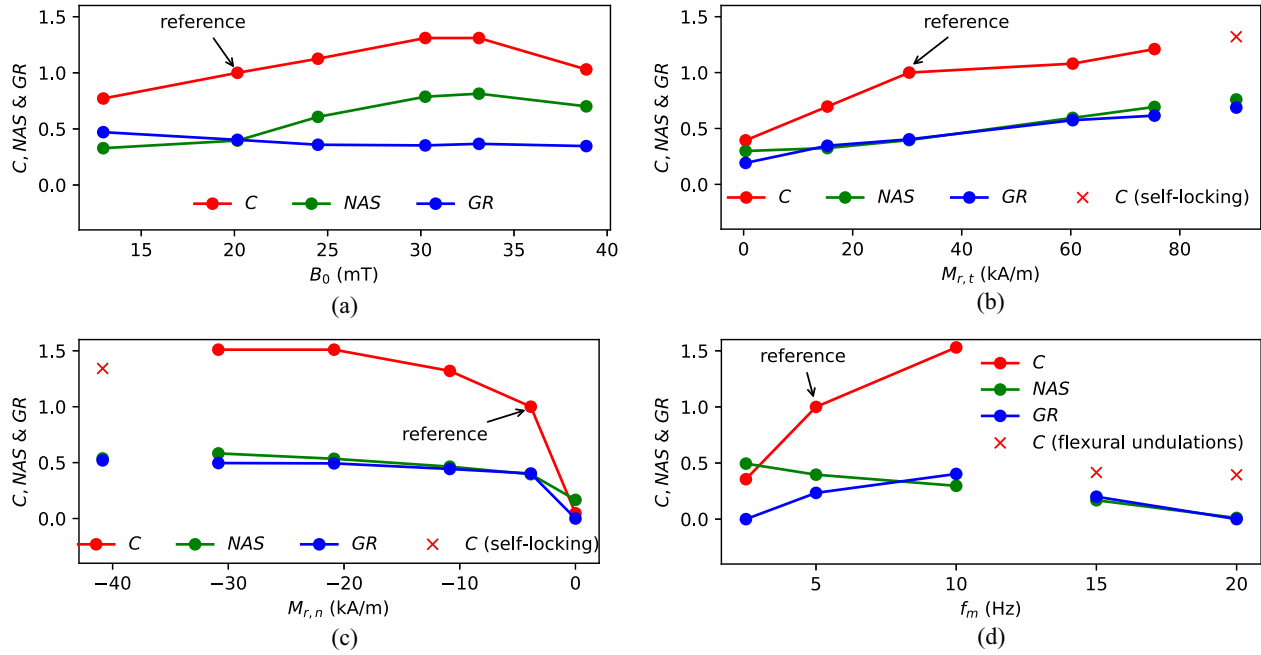


FIG. 12. Variation of C , NAS , and GR with respect to (a) B_0 , (b) $M_{r,t}$, (c) $M_{r,n}$, and (d) f_m .

C. Magnetics

We vary the range of the magnetic field B_0 to understand its influence on the swimming performance. The absolute difference between the maximum and minimum values of B_0 for the temporal variation during one swimming cycle denotes the range of B_0 . For the reference case [see Fig. 2(b)], the value of this range is approximately 20 mT (as shown in Fig. 12). By increasing B_0 , the jellyfishbots traverse greater distances and exhibit enhanced average speeds due to higher actuating loads. This is due to the increase in lappet deformation, and larger swept areas of the lappet tip. However, we observe this trend only until a certain value of B_0 , which is approximately 30.5 mT [see Fig. 12(a)]. We refer to this value of B_0 as the optimum value of the magnetic actuation. Beyond this, the jellyfishbot swimming performance decreases. This is due to the extreme magnetoresponsiveness and large deformation of the magnetic composite elastomeric lappets, which lets them suck up the surrounding fluid in the subumbrella region and move backward (downward) during the relaxation phase. This also reduces the spatial as well as the temporal

asymmetry, thereby leading to a further decrease in the jellyfishbot swimming performance. Also, extreme cases of shape morphing render the jellyfishbot vulnerable to self-locking.

The tangential ($M_{r,t}$) and normal ($M_{r,n}$) components of the magnetization vector are written as a linear combination of trigonometric and constant functions [see Eq. (8) and Fig. 2(a)]:

$$M_r = M_0 + M_1 \sin(\phi) + M_2 \cos(\phi). \tag{8}$$

M_0 , M_1 , and M_2 take default values of -30.37 , -2.23 , and 32.12 kA/m, respectively, for $M_{r,t}$ (for the left lappet). For the right lappet, M_0 , M_1 , and M_2 take default values of 30.37 , 2.23 , and -32.12 kA/m, respectively. Similarly, the respective reference values are -3.86 , -26.25 , and -53.75 kA/m in the case of $M_{r,n}$ (see [68] for details). Here, ϕ is mathematically defined as a product of the phase (of M_r along the lappet length, equal to 3.0 for the reference case), and the normalized distance (\bar{s}) of each node from the jellyfishbot center [refer to Eq. (9)]. The phase is dimensionless and so is \bar{s} . The latter is zero at the jellyfishbot center

TABLE I. Influence of relative contribution of the relaxation, contraction, and glide phases, upon the jellyfishbot displacement per cycle and average speed.

| Identity | Relaxation phase (%) | Contraction phase (%) | Glide phase (%) | Ratio | c (mm/s) | C |
|---------------------|----------------------|-----------------------|-----------------|-----------|------------|------|
| S1 (reference case) | 30 | 48.3 | 21.7 | 1.4:2.2:1 | 2.07 | 1 |
| S2 | 60 | 18.335 | 21.665 | 3.3:1:1.2 | 2.19 | 1.06 |
| S3 | 10 | 45 | 45 | 1:4.5:4.5 | 2.33 | 1.13 |
| S4 | 40 | 20 | 40 | 2:1:2 | 2.17 | 1.05 |
| S5 | 30 | 21.7 | 48.3 | 1.4:1:2.2 | 2.22 | 1.07 |
| S6 | 15 | 15 | 70 | 1:1:4.7 | 1.53 | 0.74 |
| S7 | 33.3 | 33.3 | 33.4 | 1:1:1 | 2.31 | 1.12 |
| S8 | 50 | 0 | 50 | 1:0:1 | 2.36 | 1.14 |
| S9 | 0 | 50 | 50 | 0:1:1 | 2.26 | 1.09 |

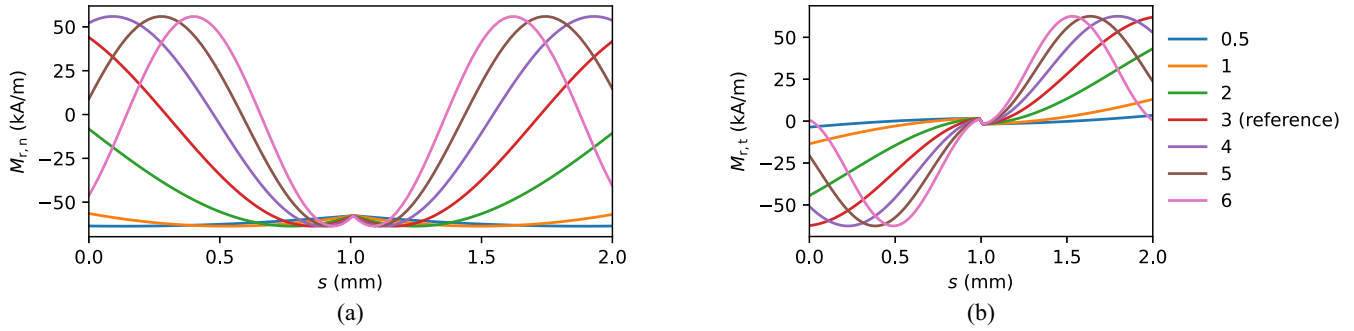


FIG. 13. Variation of (a) $M_{r,n}$ and (b) $M_{r,t}$ along the curvilinear axis s of the swimmer for different values of the phase.

(corresponding to $s = 1$ mm) and 1 at the end [corresponding to $s = 2$ mm in Fig. 2(a)].

$$\phi = \text{phase} * \bar{s}. \quad (9)$$

The remnant magnetization (or, remanence) is a measure of the magnetization in a material when the driving magnetic field is zero. The difference between this value and the saturation magnetization is assumed to be negligible even under the application of external magnetic fields [68]. In other words, the magnetization is assumed to be independent of the value of B_0 [69].

With this underlying assumption, we study the influence of the magnitude of the remnant magnetization (M_r). In particular, we vary only its fixed component (M_0), individually for $M_{r,t}$ and $M_{r,n}$, and observe its influence upon the jellyfishbot swimming kinematics. With the increase in M_0 for $M_{r,t}$, the magnetoresponsiveness of the jellyfishbot lappets increases, and the time taken to respond to the change in the external field reduces consequently. Thus, the jellyfishbot swimming kinematics improves [see Fig. 12(b)]. However, at a certain value of M_0 for $M_{r,t}$, we observe that the deformation of the flexible jellyfishbot becomes so large that it leads to self-locking, which prohibits it from swimming further after the first cycle. Thus, too high or low a value of M_0 for $M_{r,t}$ reduces the jellyfishbot swimming efficiency, and we have to choose an intermediate for this magnetic property from Fig. 12(b).

The effect of $M_{r,n}$ is discussed in Fig. 12(c). Here, the effect is the opposite compared to that for $M_{r,t}$: increasing $M_{r,n}$ (approaching zero, and then beyond) leads to a decrease in the swimming performance. Also, too high a negative value of $M_{r,n}$ leads to excessive lappet deformation and self-locking. As a result, we have to choose an intermediate value for

optimal swimming behavior, i.e., approximately -25 kA/m [from Fig. 12(c)].

It is important to note that when either the magnetic field or the remnant magnetization is very high, the lappet deformation is high, inducing self-locking. Only when the magnetic field is reduced or the next swimming cycle starts, the lappets return to their relaxed state through an uncharacteristic spring-back lappet motion. As also explained in Sec. IV B, we refer to this intermediate locked structure obtained during self-closure of the deformable lappets as “self-locking” [refer Fig. 11(b)].

Next, we analyze the effect of actuation frequency (f_m) upon the jellyfishbot swimming kinematics. In doing so, the ratio of the individual phases is kept the same for all the numerical simulations performed, unless otherwise mentioned. The relaxation, contraction, and glide phases account for 30, 48.3, and 21.7% of t_{ref} , respectively.

Until a certain value of f_m , we note that the jellyfishbot speed increases with an increase in the actuation frequency. There is a time lag between the two cycles, which decreases when f_m increases. This time lag manifests itself in the glide phase, which effectively enhances the jellyfishbot speed. However, beyond a certain value, the swimming speed reduces [see Fig. 12(d)].

It is observed that as f_m increases, the jellyfishbot travels shorter distances per cycle with low speeds since the actuation load (per unit time) it receives per cycle decreases. For frequencies larger than 10 Hz, the jellyfishbot deforms very fast, and in an undulating manner, akin to a soft vibrating beam or string. The jellyfishbot does not progress forward, and its vertical displacement per swimming cycle is negligible. In addition, the contribution from the glide reduces to a negligible quantity.

The jellyfishbot can ideally be perceived as a (vertically) actuated cantilever beam, vibrating in a frequency range of 2–20 Hz in mode shape 1. The lappet deformation is analogous to the first mode deformation for a cantilever beam, which corresponds to the (first) eigenfrequency $f_n = 3.52 \sqrt{\frac{EI}{\rho AL^4}}$. Plugging in the default parameter values (as considered for the reference case), f_n is calculated to be 71.64 Hz. We notice that this value of f_n is already considerably higher than the operating range of frequencies in the present paper (maximally 20 Hz), so that resonance will not occur in the absence of viscous damping, let alone in the presence of damping.

The relative contribution of the three phases (relaxation, contraction, and glide) in a swimming jellyfishbot and its

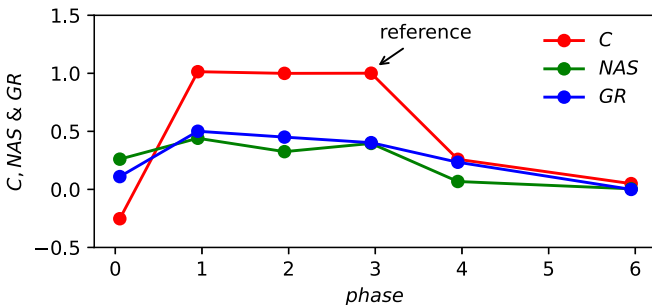


FIG. 14. Variation of C , NAS , and GR with respect to phase.

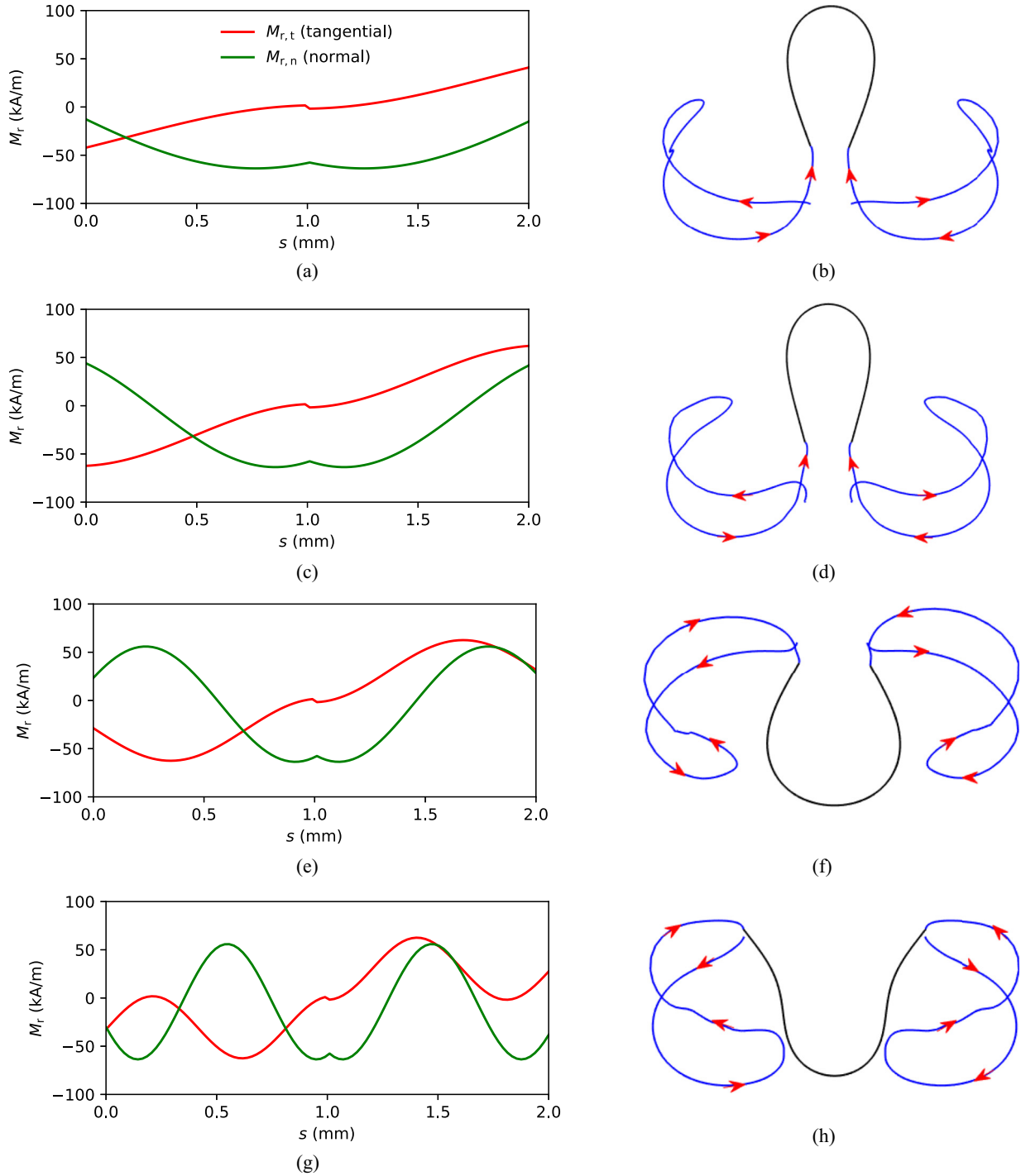


FIG. 15. Variation of the remnant magnetization M_r with respect to the curvilinear axis s for different values of phase, and the corresponding lappet trajectories: (a) phase = 1.875 (beam mode 1), (b) phase = 3, (c) phase = 4.694 (beam mode 2), and (d) phase = 7.855 (beam mode 3).

forward propulsion is discussed now while keeping the frequency the same. Its effect on the average swimming speed is reported in Table I. We observe that the swimmer S8 has the highest value of C . All jellyfishbots except S6 exhibit a minimum average speed of 2.0 mm/s. For S6, the relaxation and contraction phases are equal and considerably lower than the glide phase (Table I). The variation in the duration of individual phases gives rise to their individual dominance.

Not only the magnitude of the remnant magnetization M_r (as discussed earlier) but also its variation along the curvilinear length s for different values of the phase [see Figs. 13(a) and 13(b)] affects the jellyfishbot kinematic performance. The phase of M_r dictates its periodicity. This affects the jellyfishbot lappet deformation and, consequently, the NAS and C . With an increase in the phase, C improves to an optimum value in the range 1–3, after which C starts to decrease (see

TABLE II. Variation of jellyfishbot swimming efficiency for different fluids subject to a change in the external actuation frequency or flexural rigidity per unit out-of-plane thickness.

| Fluid system | μ (Pa s) | f_m (Hz) | EI (Pa m ³) | k (prefactor for \mathbf{B}_0) | C |
|-----------------|--------------|------------|---------------------------|-------------------------------------|------|
| Castor oil | 0.25 | 10 | 4.58 | 1.5 | 0.76 |
| | | 10 | 4.12 | 1.5 | 0.87 |
| | | 10 | 3.43 | 1.5 | 0.85 |
| Reference fluid | 0.1 | 10 | 4.23 | 1.0 | 1.75 |
| | | 5 | 4.23 | 1.0 | 1 |
| Vegetable oil | 0.035 | 10 | 4.58 | 1.5 | 1.76 |
| | | 10 | 13.39 | 1.5 | 1.02 |
| | | 10 | 6.52 | 1.5 | 1.57 |
| | | 5 | 5.72 | 1.2 | 1.78 |
| | | 5 | 3.6 | 1.2 | 0.81 |
| | | 5 | 4.58 | 1.2 | 1.71 |
| | | 5 | 6.52 | 1.2 | 0.65 |
| | | 5 | 11.10 | 1.2 | 1.20 |
| Blood | 0.004 | 5 | 4.58 | 0.8 | 1.28 |
| | | 5 | 5.72 | 0.8 | 0.99 |
| Water | 0.0008 | 5 | 12.24 | 0.7 | 1.10 |
| | | 5 | 13.39 | 0.7 | 0.80 |

Fig. 14). A phase value of approximately 3 is observed to bring out the best jellyfishbot kinematics because then the lappets sweep the highest possible area per swimming cycle for the lappet deformation.

Different mode shapes characterized by varying the phase correspond to specific trajectories. The lappets displace different quantities of the surrounding fluid, leading to distinct swept areas, resulting in different values of C . The lappet trajectories for different values of phase (that characterize the different mode shapes [70]) are shown in Figs. 15 and 16. For a phase of approximately 2, the lappet deformation is equivalent to the first mode shape of an Euler-Bernoulli beam, while for other phase values, we observe higher mode shapes. These higher mode shapes sweep lower areas per swimming cycle, because of the additional curvature along the lappet length (see Figs. 15 and 16). A phase value of 3 sweeps the maximum area, thereby giving rise to optimal jellyfishbot kinematics.

Finally, we systematically vary $M_{r,t}$ as well as $M_{r,n}$ to understand its effect upon the lappet trajectory and NAS in Figs. 17 and 18, respectively. As discussed in Fig. 16, where the phase was varied, here we manipulate the magnitude (M_0) of the remnant magnetization components ($M_{r,t}$ and $M_{r,n}$) to

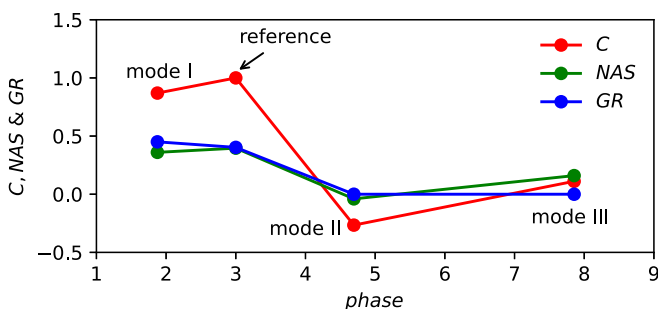


FIG. 16. Variation of C , NAS , and GR with respect to the phase for different modes (i.e., lappet deformation).

observe their influence upon the lappet trajectory during one swimming cycle. We find that all the lappet trajectories are distinct dumbbell-shaped closed loops with a strong similarity to the reference lappet trajectory (see Fig. 8). The value of NAS , which is an important parameter that determines the overall jellyfishbot swimming kinematics, keeps increasing with the value of the remnant magnetization component.

D. Parameter optimization

In this subsection, we bring together our observations and understanding from the previous sections to analyze some real-life cases, wherein the jellyfishbot is assumed to traverse through some viscous fluid under the application of an external magnetic field. We will choose specific values of the different system parameters with the objective to achieve the best swimming performance. There always exists a competition between the magnetic, elastic, and viscous forces, and their interplay and relative dominance dictate the overall jellyfishbot swimming kinematics.

We assume the fluid properties (μ , ρ_f) and the magnetic properties (\mathbf{M}_r) of the swimmer to be constant and optimize the structural properties (flexural rigidity EI) of the swimmer and the applied magnetic field (\mathbf{B}_0 , f_m). There is the freedom to choose the value of lappet stiffness (or the lappet thickness) to manipulate the flexural rigidity required to maximize the net area swept for enhanced forward propulsion. Alternatively, we can change the magnitude and frequency of the applied external magnetic field. For the present analysis of jellyfishbot swimming performance and design optimization, the following fluids are chosen: water, blood, vegetable oil, the reference fluid, and castor oil.

We explain the design strategy to optimize c for a given fluid through Table II. To begin with, let us first optimize c in the case of a highly viscous fluid, castor oil. Here, the fluid viscosity is very high, which leads to increased resistance during lappet deformation. Thus, the swept area decreases

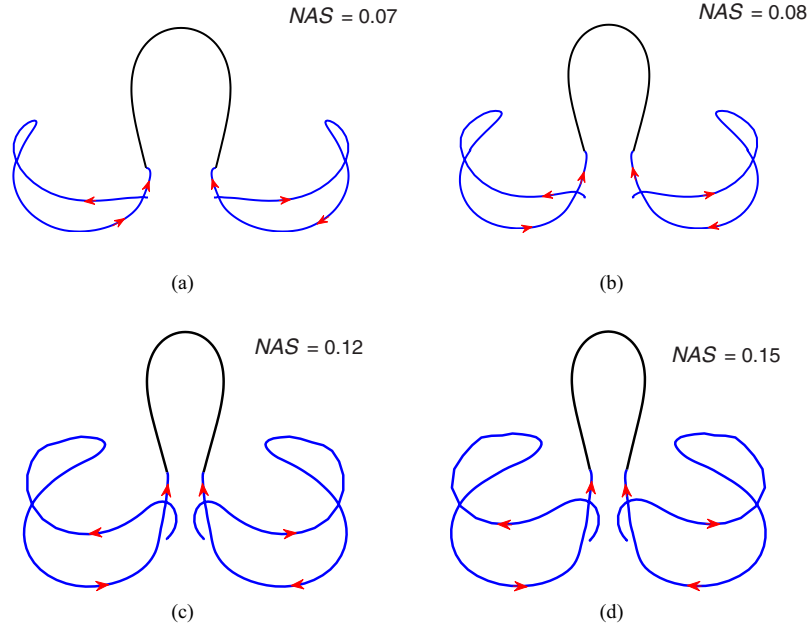


FIG. 17. Schematic representation of the lappet trajectories (for one swimming cycle) and the corresponding NAS for different values of $M_{r,t}$: (a) 0.37 kA/m, (b) 15.37 kA/m, (c) 45.37 kA/m, and (d) 60.37 kA/m.

and this leads to a lower value of c . To compensate for that, we decrease the value of EI to 4.12 Pa m^3 and observe that the lappets deform sufficiently enough to generate the thrust required for forward propulsion.

Since the viscosity is high, the glide phase has less contribution; hence, we would like to lower the time for glide and we do so by increasing the external actuation frequency to 10 Hz. Thus, the swimmer starts off the next cycle without wasting the glide time without covering any noticeable distance. Finally, to compensate again for the in-

creased viscous forces due to the enhanced frequency, we increase the magnetic field by a prefactor (k) of 1.5 in order to ensure considerable lappet deformation. However, despite this optimization procedure, the maximal swimming velocity is smaller than that of the reference swimmer (see Table II).

Let us now discuss the scenario when the surrounding fluid is either blood or water (a low-viscosity fluid). Here, the jellyfishbot lappets experience minimum fluid resistance or hindrance to their flexural deformation. Hence, they are

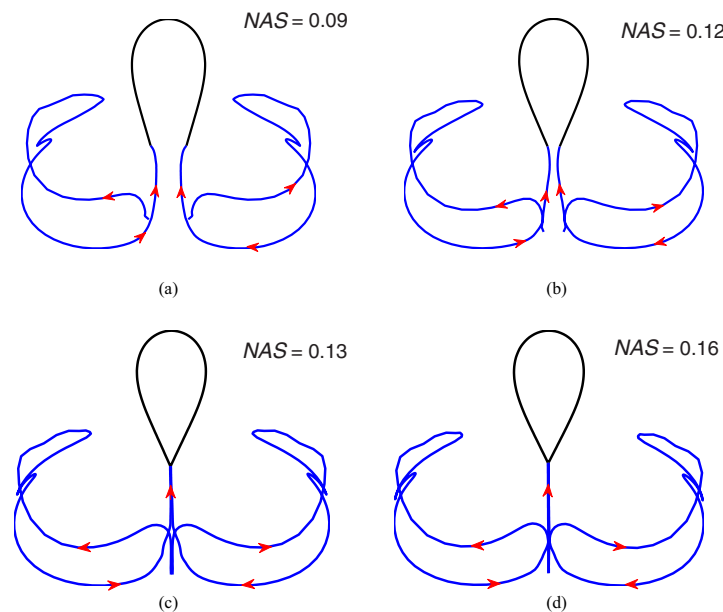


FIG. 18. Schematic representation of the lappet trajectories (for one swimming cycle) and the corresponding NAS for different values of $M_{r,n}$: (a) 0.86 kA/m, (b) 10.86 kA/m, (c) 20.86 kA/m, and (d) 30.86 kA/m.

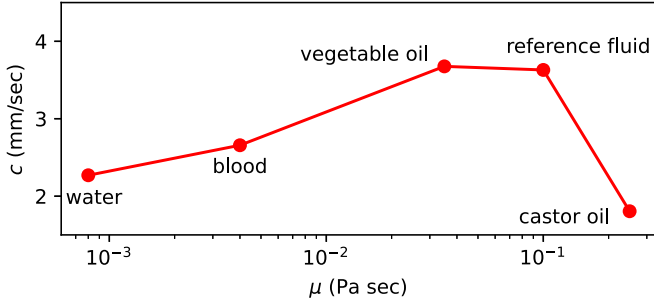


FIG. 19. Optimized jellyfishbot swimming speed for a wide range of viscous fluids.

very prone to early lappet closure and self-locking. Hence, we increase the flexural rigidity to a higher value so as to minimize the chance of lappet closure. However, this also brings with it the chance of higher flexural vibration and low glide, as discussed earlier. Of course, the increase in flexural rigidity should remain modest so as not to sweep a lower area. Also, the external magnetic field is reduced using prefactors k of 0.8 and 0.7 (for blood and water, respectively) to limit lappet deformation. Using combinations of changing magnetic field and flexural rigidity, it follows that, despite the much-lower viscosity, the swimming performance cannot be increased compared to the reference case, as can be seen in Fig. 19.

However, as can be deduced from Fig. 19, for vegetable oil, the viscosity is neither too high nor too low. Rather, it allows for considerable lappet deformation and since the fluid viscosity is not too high, the swimmer can glide through the fluid to cover the extra distance in the glide phase (due to temporal asymmetry). Both these aspects add to an increase in the value of c . In this case, the optimal system parameters are quite similar to that for the reference case (see Fig. 1); only the magnetic field is increased by factors of 1.2 and 1.5 (for 5 and 10 Hz, respectively) and the flexural rigidity takes a value of 5.72 Pa m^3 .

For a multiphysics problem such as this, there are ten different system parameters that need to be optimized in order to maximize the overall swimming kinematics. In essence, this would require a multiobjective optimization methodology with ten functional dependencies and several constraints as well, which would require very high computational costs and resources. Instead, we followed an intuitive, mechanics-based optimization procedure to strike out the ideal balance between the elastic, magnetic, and viscous forces so that a maximal jellyfishbot swimming speed is achieved. Alternatively, to reduce the number of independent parameters, a dimensional analysis can be performed. This is the topic of the next section.

V. NONDIMENSIONAL NUMBERS AND KINEMATICS

We have a total of ten independent system parameters, which take into account the effects of solid dynamics, fluid mechanics, and magnetics (ρ , ρ_f , L , W , h , E , t_{ref} , μ , M_r , B_0). Here, H represents the channel width (see Fig. 1). From here on, we assume the phase to have a constant value of 1 throughout. We also change only the value of M_0 (for both $M_{r,t}$ and $M_{r,n}$) when we vary M_r ; i.e., the values of M_1 and M_2 are held constant. There are four mutually independent base dimensions: mass (M), length (L), time (T), and ampere (A).

Following the Buckingham- π theorem, we, therefore, have a total of six nondimensional terms.

A. Nondimensional numbers

The kinematic response of the jellyfishbot is characterized using the following nondimensional numbers [62]: the fluid number (ratio of viscous to elastic forces) $F_n = 12\mu L^3/Eh^3 t_{\text{ref}}$, the inertia number (ratio of jellyfishbot inertia forces to elastic forces) $I_n = 12\rho L^4/Eh^2 t_{\text{ref}}^2$, the magnetic number (the ratio of magnetic forces to elastic forces) $M_n = 12M_r B_0 L^2/Eh^2$, the flapping Reynolds number (the ratio of inertia forces to viscous forces in the fluid) $R_n = \rho_f L^2/\mu t_{\text{ref}}$, the diffusion Reynolds number (the ratio of momentum diffusion time to the jellyfishbot swimming cycle time) $D_n = \rho_f (W - L)^2/\mu t_{\text{ref}}$, and the mass number $M = \rho/\rho_f$.

During the effective and recovery strokes, the jellyfishbot lappets push the fluid around it and propel it forward. The momentum generated due to the jellyfishbot locomotion diffuses from this region towards the channel walls. The relevant length scales are L and $W - L$, and the relevant time scale is t_{ref} . D_n signifies how long it takes for the momentum (gained by the fluid due to jellyfishbot lappet motion) to further diffuse into the fluid, whereas R_n quantifies the relative dominance of the fluid inertia and viscous forces.

In our paper, the Reynolds number typically varies from 0.3 to 0.6. As a result, we observe a relatively low glide phase for the jellyfishbot because the chosen default value of fluid viscosity is relatively high (0.9 Pa s). However, for lower values of fluid viscosity and thus a higher Reynolds number, inertial effects will have a more prominent role during gliding. This has been explained in the authors' earlier work [67], which shows a considerable glide phase at a higher Reynolds number of 6.75.

The six nondimensional numbers mentioned above completely capture the physical behavior of the jellyfishbot and the generated propulsion speed, which can be summarized as $C = C(F_n, I_n, M_n, R_n, D_n, M)$. From the data, we observe a maximal correlation of C with I_n , M_n , and R_n . Hence, we focus only on I_n , M_n , and R_n in Fig. 20(a).

It thus appears that the solid mechanics, fluid dynamics, and magnetics describing the kinematics of the jellyfishbot are best represented by I_n , M_n , and R_n . We, therefore, devise a dimensionless number Y_n that has a power-law relationship with I_n , M_n , and R_n . We observe that Y_n has an increasing trend with C [as shown in Fig. 20(a)] and is thus capable of describing the jellyfishbot kinematics as a function of most of the system variables with a reasonably good correlation.

B. Kinematic correlations

There are two key kinematic contributions to the swimming efficiency of jellyfishbots: (i) the effect of spatial asymmetry represented by the swept area of the jellyfish lappets and (ii) the effect of temporal asymmetry represented by the glide phase. We, therefore, make an endeavor in this section to collect the data from all the numerical simulations (similar to the data used in the previous section) and investigate the functional dependence of C upon GR and NAS.

From the data, we learn that high values of both NAS and GR together give rise to enhanced values of C as both

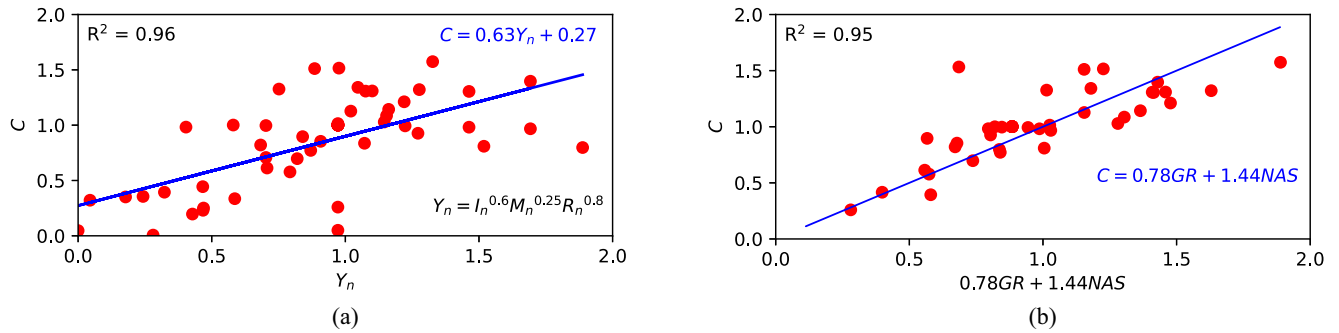


FIG. 20. (a) Correlation of C with a power-law combination of I_n , M_n , and R_n . (b) Correlation of C with a linear combination of GR and NAS.

the spatial and temporal symmetry contribute to the jellyfishbot locomotion. To capture that, the relative influence of both NAS and GR upon C is studied by assuming a linear combination, showing that the dependence on NAS is a factor 2 larger than on GR [see Fig. 20(b)]. Clearly both jellyfishbots and their living counterparts utilize the physics of spatiotemporal symmetry breaking during their versatile locomotion and adaptive FSI when swimming through a viscous fluid.

Finally, we discuss the feasibility of the jellyfishbot considered in the present paper for real-life applications. Our reference jellyfishbot has a characteristic size of 2.0 mm, and the typical diameter of human blood vessels varies from a few micrometers (for capillaries) to approximately around 25 mm (for the human aorta [71]). The arteries and veins have a slightly higher diameter ($\approx 4\text{--}5$ mm). Therefore, the model jellyfishbot could ideally swim through the veins, arteries, and aorta, but not the capillaries (for which we require miniaturization of the model jellyfishbot). Nonetheless, the jellyfishbot could potentially cater to several biomedical applications as well, such as endoscopy, laparoscopy, and a gastroretentive drug delivery system and gastrointestinal tract imaging, all of which have a much larger working space for the jellyfishbot to steadily swim through.

VI. CONCLUSION

In this paper, we investigated the swimming dynamics of a magnetically actuated jellyfish-inspired soft robotic swimmer by using a robust multiphysics finite-element approach that captures the magnetodynamics and large deformation fluid-structure interaction response. Compliant elastomers are impregnated with hard permanently magnetic microparticles, and the stimuli-responsive preprogrammed shape morphing allows external actuation with high precision and accuracy.

We study the coupling between the magnetic load, shape evolution, and fluid dynamics, and use these insights to computationally design an untethered compliant robotic swimmer with improved swimming performance through numerical simulation, parameter identification, and design optimization.

We observe the swimming kinematics to be influenced the most by the remnant magnetization, fluid viscosity, and lappet flexural rigidity among all system parameters. The correlation between the nondimensional average speed of the jellyfishbot and the nondimensional numbers is investigated, showing that the magnetic, inertia, and flapping Reynolds numbers are the dominant dimensionless numbers that determine the swimming performance.

In addition, we observe that the swimming speed is largest when both the spatial and temporal asymmetries contribute significantly to the jellyfishbot swimming performance. Our results provide guidelines for the design of improved jellyfish-inspired magnetic soft robotic swimmers for future microfluidic and biomedical applications, such as drug delivery, surgical devices, and carrier robots.

ACKNOWLEDGMENTS

The authors would like to thank the Center for Information Technology of the University of Groningen for their support and for providing access to the Peregrine high-performance computing cluster. The work is carried out within the research program of the Centre for Data Science and Systems Complexity, Faculty of Science and Engineering, University of Groningen. The authors would like to acknowledge the contribution of Rongjing Zhang (University of Groningen) and Prof. S. N. Khaderi (Indian Institute of Technology Hyderabad) in the initial phase of this work. Finally, the authors acknowledge helpful discussions with Prof. M. Sitti (Max Planck Institute for Intelligent Systems).

- [1] C. Majidi, Soft robotics: A perspective—current trends and prospects for the future, *Soft Robotics* **1**, 5 (2014).
- [2] D. Trivedi, C. D. Rahn, W. M. Kier, and I. D. Walker, Soft robotics: Biological inspiration, state of the art, and future research, *Appl. Bionics Biomechanics* **5**, 99 (2008).
- [3] S. Kim, C. Laschi, and B. Trimmer, Soft robotics: A bioinspired evolution in robotics, *Trends Biotechnol.* **31**, 287 (2013).

- [4] L. Lindenroth, S. Bano, A. Stilli, J. G. Manjaly, and D. Stoyanov, A fluidic soft robot for needle guidance and motion compensation in intratympanic steroid injections, *IEEE Robotics and Automation Letters* **6**, 871 (2021).
- [5] G. M. van Vliet, S. Misra, and V. K. Venkiteswaran, A magnetically-actuated flexible capsule robot for untethered cardiovascular interventions, in *2022 IEEE 5th International*

- Conference on Soft Robotics (RoboSoft)* (IEEE, New York, 2022), pp. 583–588.
- [6] J. Wang, D. Gao, and P. S. Lee, Recent progress in artificial muscles for interactive soft robotics, *Adv. Mater.* **33**, 2003088 (2021).
- [7] A. Hess, X. Tan, and T. Gao, CFD-based multi-objective controller optimization for soft robotic fish with muscle-like actuation, *Bioinspir. Biomim.* **15**, 035004 (2020).
- [8] J.-H. Hsiao, J.-Y. Chang, and C.-M. Cheng, Soft medical robotics: Clinical and biomedical applications, challenges, and future directions, *Advanced Robotics* **33**, 1099 (2019).
- [9] Z. Ren, W. Hu, X. Dong, and M. Sitti, Multi-functional soft-bodied jellyfish-like swimming, *Nat. Commun.* **10**, 2703 (2019).
- [10] Z. Ren, R. Zhang, R. H. Soon, Z. Liu, W. Hu, P. R. Onck, and M. Sitti, Soft-bodied adaptive multimodal locomotion strategies in fluid-filled confined spaces, *Sci. Adv.* **7**, eabh2022 (2021).
- [11] C. Laschi, J. Rossiter, F. Iida, M. Cianchetti, and L. Margheri, *Soft Robotics: Trends, Applications and Challenges*, Biosystems & Biorobotics (BIOSYSROB), Vol. 17 (Springer, New York, 2017).
- [12] M. Cianchetti, C. Laschi, A. Menciassi, and P. Dario, Biomedical applications of soft robotics, *Nat. Rev. Mater.* **3**, 143 (2018).
- [13] P. Thoniyot, M. J. Tan, A. A. Karim, D. J. Young, and X. J. Loh, Nanoparticle-hydrogel composites: Concept, design, and applications of these promising, multi-functional materials, *Adv. Sci.* **2**, 1400010 (2015).
- [14] H. Li, G. Go, S. Y. Ko, J.-O. Park, and S. Park, Magnetic actuated pH-responsive hydrogel-based soft micro-robot for targeted drug delivery, *Smart Mater. Struct.* **25**, 027001 (2016).
- [15] D. Rus and M. T. Tolley, Design, fabrication and control of soft robots, *Nature (London)* **521**, 467 (2015).
- [16] N. Bira, P. Dhagat, and J. R. Davidson, A review of magnetic elastomers and their role in soft robotics, *Frontiers in Robotics and AI* **7**, 588391 (2020).
- [17] N. Ebrahimi, C. Bi, D. J. Cappelleri, G. Ciuti, A. T. Conn, D. Faivre, N. Habibi, A. Hošovský, V. Iacovacci, I. S. Khalil *et al.*, Magnetic actuation methods in bio/soft robotics, *Adv. Funct. Mater.* **31**, 2005137 (2021).
- [18] A. Hajiaghajani, D. Kim, A. Abdolali, and S. Ahn, Patterned magnetic fields for remote steering and wireless powering to a swimming microrobot, *IEEE/ASME Transactions on Mechatronics* **25**, 207 (2019).
- [19] E. B. Joyee and Y. Pan, Additive manufacturing of multi-material soft robot for on-demand drug delivery applications, *J. Manufacturing Proces.* **56**, 1178 (2020).
- [20] U. Kei Cheang, K. Lee, A. A. Julius, and M. J. Kim, Multiple-robot drug delivery strategy through coordinated teams of microswimmers, *Appl. Phys. Lett.* **105**, 083705 (2014).
- [21] Y. Zhou, H. Jin, C. Liu, E. Dong, M. Xu, and J. Yang, A novel biomimetic jellyfish robot based on a soft and smart modular structure (sms), in *2016 IEEE International Conference on Robotics and Biomimetics (ROBIO)* (IEEE, New York, 2016), pp. 708–713.
- [22] Y. Kim, G. A. Parada, S. Liu, and X. Zhao, Ferromagnetic soft continuum robots, *Science Robotics* **4** (2019).
- [23] V. K. Venkiteswaran, L. F. P. Samaniego, J. Sikorski, and S. Misra, Bio-inspired terrestrial motion of magnetic soft millirobots, *IEEE Robot. Autom. Lett.* **4**, 1753 (2019).
- [24] S.-W. Yeom and I.-K. Oh, A biomimetic jellyfish robot based on ionic polymer metal composite actuators, *Smart Mater. Struct.* **18**, 085002 (2009).
- [25] T. Cheng, C. S. H. Ng, P. W. Y. Chiu, and Z. Li, Design and prototyping of a soft magnetic anchored and guidance endoscope system, in *2017 IEEE/RSJ International Conference on Intelligent Robots and Systems (IROS)* (IEEE, New York, 2017), pp. 2902–2908.
- [26] S. Fu, F. Wei, C. Yin, L. Yao, and Y. Wang, Biomimetic soft micro-swimmers: from actuation mechanisms to applications, *Biomedical Microdevices* **23**, 6 (2021).
- [27] S. Khaderi and P. Onck, Fluid-structure interaction of three-dimensional magnetic artificial cilia, *J. Fluid Mech.* **708**, 303 (2012).
- [28] S. Namdeo, S. N. Khaderi, and P. R. Onck, Swimming dynamics of bidirectional artificial flagella, *Phys. Rev. E* **88**, 043013 (2013).
- [29] N. Taketoshi, T. Omori, and T. Ishikawa, Elasto-hydrodynamic interaction of two swimming spermatozoa, *Phys. Fluids* **32**, 101901 (2020).
- [30] A. Hoover and L. Miller, A numerical study of the benefits of driving jellyfish bells at their natural frequency, *J. Theor. Biol.* **374**, 13 (2015).
- [31] R. K. Katzschmann, A. D. Marchese, and D. Rus, Hydraulic autonomous soft robotic fish for 3d swimming, in *Experimental Robotics* (Springer, New York, 2016), pp. 405–420.
- [32] A. D. Marchese, C. D. Onal, and D. Rus, Autonomous soft robotic fish capable of escape maneuvers using fluidic elastomer actuators, *Soft Robotics* **1**, 75 (2014).
- [33] X. Bi and Q. Zhu, Fluid-structure investigation of a squid-inspired swimmer, *Phys. Fluids* **31**, 101901 (2019).
- [34] H.-J. Kim, S.-H. Song, and S.-H. Ahn, A turtle-like swimming robot using a smart soft composite (ssc) structure, *Smart Mater. Struct.* **22**, 014007 (2013).
- [35] J. Frame, N. Lopez, O. Curet, and E. D. Engeberg, Thrust force characterization of free-swimming soft robotic jellyfish, *Bioinspir. Biomim.* **13**, 064001 (2018).
- [36] A. Hamidi, Y. Almubarak, Y. M. Rupawat, J. Warren, and Y. Tadesse, Poly-saora robotic jellyfish: swimming underwater by twisted and coiled polymer actuators, *Smart Mater. Struct.* **29**, 045039 (2020).
- [37] M. J. McHenry and J. Jed, The ontogenetic scaling of hydrodynamics and swimming performance in jellyfish (*aurelia aurita*), *J. Exp. Biol.* **206**, 4125 (2003).
- [38] J. C. Nawroth, H. Lee, A. W. Feinberg, C. M. Ripplinger, M. L. McCain, A. Grosberg, J. O. Dabiri, and K. K. Parker, A tissue-engineered jellyfish with biomimetic propulsion, *Nat. Biotechnol.* **30**, 792 (2012).
- [39] T. Cheng, G. Li, Y. Liang, M. Zhang, B. Liu, T.-W. Wong, J. Forman, M. Chen, G. Wang, Y. Tao *et al.*, Untethered soft robotic jellyfish, *Smart Mater. Struct.* **28**, 015019 (2019).
- [40] Z. Ren, T. Wang, W. Hu, and M. Sitti, A magnetically-actuated untethered jellyfish-inspired soft milliswimmer, in *Robotics: Science and Systems XV*, edited by A. Bicchi, H. Kress-Gazit, and S. Hutchinson (Max Planck Institute, Germany, 2019).
- [41] M. A. Kazemi-Lari, A. D. Dostine, J. Zhang, A. S. Wineman, and J. A. Shaw, in *Bioinspired Sensing, Actuation, and Control in Underwater Soft Robotic Systems* (Springer, New York, 2021), pp. 171–187.

- [42] A. Joshi, A. Kulkarni, and Y. Tadesse, Fludojelly: experimental study on jellyfish-like soft robot enabled by soft pneumatic composite (spc), *Robotics* **8**, 56 (2019).
- [43] I. S. Khalil, A. F. Tabak, M. Abou Seif, A. Klingner, and M. Sitti, Controllable switching between planar and helical flagellar swimming of a soft robotic sperm, *PLoS ONE* **13**, e0206456 (2018).
- [44] B. Gamus, L. Salem, E. Ben-Haim, A. D. Gat, and Y. Or, Interaction between inertia, viscosity, and elasticity in soft robotic actuator with fluidic network, *IEEE Transactions on Robotics* **34**, 81 (2017).
- [45] Z. Zhou and R. Mittal, Computational modeling of swimming in marine invertebrates with implications for soft swimming robots, *Bioinspir. Biomim.* **15**, 046010 (2020).
- [46] W. Huang, Z. Patterson, C. Majidi, and M. K. Jawed, Modeling soft swimming robots using discrete elastic rod method, in *Bioinspired Sensing, Actuation, and Control in Underwater Soft Robotic Systems* (Springer, New York, 2021), pp. 247–259.
- [47] Y. Mirzae, B. Y. Rubinstein, K. I. Morozov, and A. M. Leshansky, Modeling propulsion of soft magnetic nanowires, *Frontiers in Robotics and AI* **7**, 595777 (2020).
- [48] W. Gao and X. Wang, Conceptual design and multifield coupling behavior of magnetically propelled fish-like swimmers, *Smart Mater. Struct.* **29**, 114007 (2020).
- [49] S. Khaderi, C. Craus, J. Hussong, N. Schorr, J. Belardi, J. Westerweel, O. Prucker, J. Rühle, J. Den Toonder, and P. Onck, Magnetically-actuated artificial cilia for microfluidic propulsion, *Lab Chip* **11**, 2002 (2011).
- [50] H. Ye, Y. Li, and T. Zhang, Magttice: A lattice model for hard-magnetic soft materials, *Soft Matter* **17**, 3560 (2021).
- [51] S. Khaderi, J. Den Toonder, and P. Onck, Magnetically actuated artificial cilia: The effect of fluid inertia, *Langmuir* **28**, 7921 (2012).
- [52] S. N. Khaderi, J. M. den Toonder, and P. R. Onck, Magnetic artificial cilia for microfluidic propulsion, *Adv. Appl. Mech.* **48**, 1 (2015).
- [53] R. van Loon, P. D. Anderson, F. N. van de Vosse, and S. J. Sherwin, Comparison of various fluid–structure interaction methods for deformable bodies, *Comput. Struct.* **85**, 833 (2007).
- [54] R. D. Cook, D. S. Malkus, M. E. Plesha, and R. J. Witt, *Concepts and Applications of Finite Element Analysis* (Wiley, New York, 2007).
- [55] L. E. Malvern, *Introduction to the Mechanics of a Continuous Medium*, Monograph (Prentice-Hall, Inc., Englewood Cliffs, NJ, 1969).
- [56] R. Annabattula, W. Huck, and P. Onck, Micron-scale channel formation by the release and bond-back of pre-stressed thin films: A finite element analysis, *J. Mech. Phys. Solids* **58**, 447 (2010).
- [57] N. M. Newmark, A method of computation for structural dynamics, *J. Eng. Mech. Div.* **85**, 67 (1959).
- [58] M. Bradford and N. A. Yazdi, A Newmark-based method for the stability of columns, *Comput. Struct.* **71**, 689 (1999).
- [59] K. Subbaraj and M. Dokainish, A survey of direct time-integration methods in computational structural dynamics. ii. Implicit methods, *Comput. Struct.* **32**, 1387 (1989).
- [60] G. Noh and K.-J. Bathe, For direct time integrations: A comparison of the Newmark and $\rho\infty$ -bathe schemes, *Comput. Struct.* **225**, 106079 (2019).
- [61] H. Hashamdar, Z. Ibrahim, and M. Jameel, Finite element analysis of nonlinear structures with Newmark method, *Int. J. Phys. Sci.* **6**, 1395 (2011).
- [62] S. N. Khaderi, M. G. H. M. Baltussen, P. D. Anderson, D. Ioan, J. M. J. den Toonder, and P. R. Onck, Nature-inspired microfluidic propulsion using magnetic actuation, *Phys. Rev. E* **79**, 046304 (2009).
- [63] K.-J. Bathe, H. Zhang, and S. Ji, Finite element analysis of fluid flows fully coupled with structural interactions, *Comput. Struct.* **72**, 1 (1999).
- [64] R. van Loon, P. D. Anderson, and F. N. van de Vosse, A fluid–structure interaction method with solid-rigid contact for heart valve dynamics, *J. Comput. Phys.* **217**, 806 (2006).
- [65] See Supplemental Material at <http://link.aps.org/supplemental/10.1103/PhysRevE.107.014607> for animations of the swimmer.
- [66] K. Feitl, A. Millett, S. Colin, J. O. Dabiri, and J. H. Costello, Functional morphology and fluid interactions during early development of the scyphomedusa aurelia aurita, *Biol. Bull.* **217**, 283 (2009).
- [67] R. Pramanik, P. R. Onck, and R. W. C. P. Verstappen, Bi-directional locomotion of a magnetically-actuated jellyfish-inspired soft robot, in *Advances in Robotics-5th International Conference of The Robotics Society* (ACM, 2021), pp. 1–5.
- [68] W. Hu, G. Z. Lum, M. Mastrangeli, and M. Sitti, Small-scale soft-bodied robot with multimodal locomotion, *Nature (London)* **554**, 81 (2018).
- [69] S. N. Khaderi, Nature-inspired microfluidic propulsion using magnetic artificial cilia, Ph.D. thesis, University of Groningen, 2011.
- [70] B. A. Zai, M. Park, S.-C. Lim, J.-W. Lee, and R. A. Sindhu, Structural optimization of cantilever beam in conjunction with dynamic analysis, in *Proceedings of the Computational Structural Engineering Institute Conference* (Computational Structural Engineering Institute of Korea, 2008), pp. 397–401.
- [71] B. Müller, S. Lang, M. Dominietto, M. Rudin, G. Schulz, H. Deyhle, M. Germann, F. Pfeiffer, C. David, and T. Weitkamp, High-resolution tomographic imaging of microvessels, in *Developments in X-Ray Tomography VI*, Proc. SPIE 7078, Vol. 70780B (SPIE, Bellingham, WA, 2008), pp. 89–98.